Biochemical Engineering Journal 181 (2022) 108415

Contents lists available at ScienceDirect

Biochemical Engineering Journal

journal homepage: www.elsevier.com/locate/bej

Modeling-based design specifications for microfluidic gradients generators for biomedical applications

Sara Micheli [a,b,1], Paolo Mocellin [a,1], Marco Sorgato [a], Lorenzo Bova [a,b], Elisa Cimetta [a,b,*]

[a] University of Padua, Department of Industrial Engineering (DII), 35131 Padova, Italy
[b] Fondazione Istituto di Ricerca Pediatrica Città della Speranza (IRP), Corso Stati Uniti 4, 35127 Padova, Italy

ARTICLE INFO

Keywords:
Bioreactor
Microfluidics
Computational Fluid Dynamics
Gradient generator

ABSTRACT

This work proposes a comprehensive approach to optimize the design of microfluidic concentration gradient generators (MGGs) for biomedical applications. Exposing biological systems to controlled gradients enables fast screenings of induced concentration-dependent signals and surpasses several limitations of conventional cell culture techniques. The MGG working principle is the formation of diffusion-driven concentration gradients between a source and a sink, both connected to a cell culture chamber through an array of microchannels. The devices were modeled with Comsol Multiphysics®, in a combined fluid-dynamic and mass-transport study allowing prediction of the internal fields and guiding design optimization. Ideal MGGs must ensure fast transients (< 1 h) to reach a steady gradient. To identify the key features determining the device performance, we analyzed design specifications and operating parameters including: the shape of the source and sink (width 1–2 mm), the number and length of the microchannels (17–34, and 2.5–5 mm), the flow rate (5–10 µl/min). Our results prove that the formation and shape of the gradient are strongly affected by the device geometry, and mostly by the microchannels length. In addition, higher flow rates lead to the generation of stagnation zones and increase the gradient steepness. The model optimized MGG was fabricated and proved successful in the generation of stable concentration gradients over cell monolayers inside the culture chamber.

1. Introduction

Inside our bodies, concentration gradients of biomolecules, gases, and chemicals, are essential to regulate several biological processes and cell functions including development, embryogenesis, and cancer metastasis [1]. Our cells evolved to recognize the directional information encoded in gradients, and translate it into processes such as neuron guidance, recruitment of immune cells, and angiogenesis. Traditional methods like Boyden chambers and collagen matrices are strongly limited by the spatial and temporal instability of the gradients they generate. Moreover, their relatively large dimensions are not ideal for a precise control [2,3].

The use of microscale devices for the generation of controllable and stable concentration gradients is beneficial for many reasons. First, the miniaturization of channel sizes in a microfluidic gradient generator (MGG), directly correlates with a reduction of the time required to transport specific concentration doses to cells, providing physiologically meaningful time scales. MGGs also enable the integration and manipulation of multiple design parameters such as time, chemical species, and concentration into a single platform. Finally, the use of small quantities of reagents and materials minimizes all operational costs.

MGG can be assimilated to reactors in which the desired concentration field is defined across a region of the device [4,5]; this generalization makes them amenable to be adapted to several experimental needs and applications. If an increased throughput and/or parallelization are required, integrated platforms composed of several gradient reactors can be assembled in series or parallel configurations. For example, Rho and co-authors [6] discussed an array of 16 parallel mixing reactors for pH gradient generation, while others [5] chose a configuration in series for the control of concentration fields across a defined range. Parallel microreactors can also be integrated to expose biological substrates to a vast combination of concentration patterns [7,8]. While highlighting the versatility of microreactors, researchers must be aware of some limitations, including possible concentration uniformity issues and controllability of configurations for high throughput

* Corresponding author at: University of Padua, Department of Industrial Engineering (DII), 35131 Padova, Italy.
E-mail address: elisa.cimetta@unipd.it (E. Cimetta).
[1] Equally contributing authors.

https://doi.org/10.1016/j.bej.2022.108415
Received 15 October 2021; Received in revised form 21 March 2022; Accepted 23 March 2022
Available online 26 March 2022

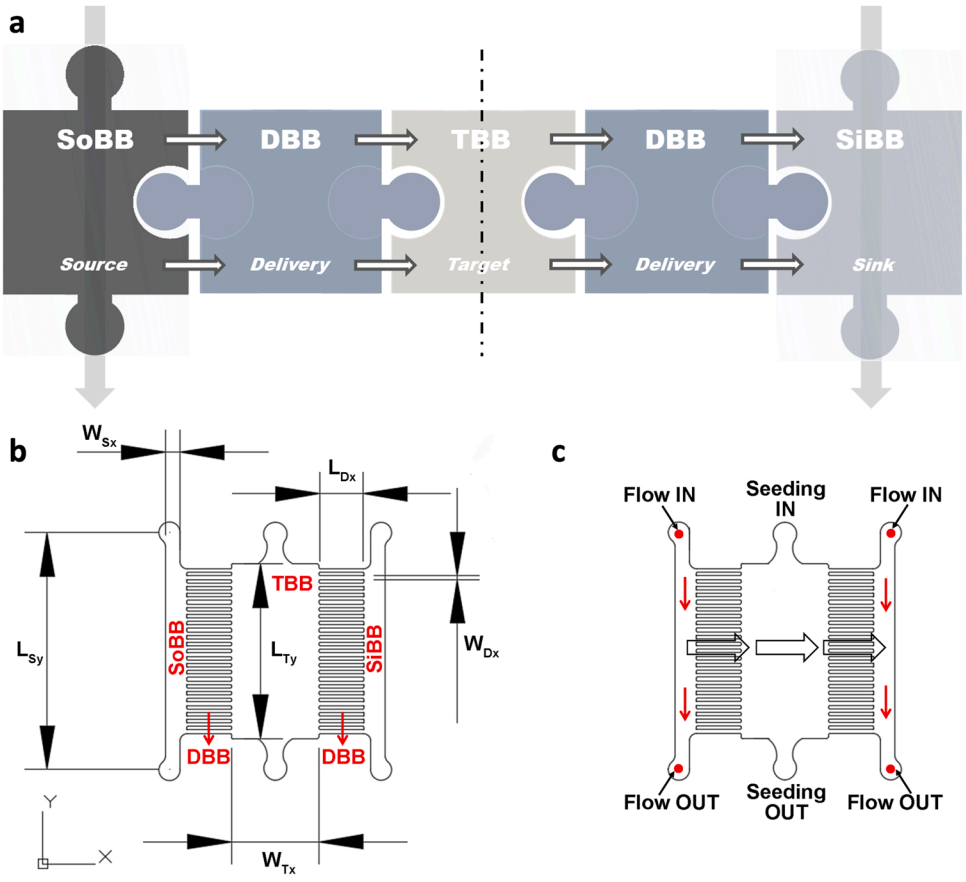

Fig. 1. Proposed MGG design. a. Building blocks of a general MGG. SoBB: source building block; DBB: delivery building block; TBB: target building block (cell culture chamber); SiBB: sink building block. Arrows indicate the dominant direction of transport phenomena in the associated microdevice: vertical for convection, horizontal for diffusion. b. Fabricated device with geometrical variables and building blocks clearly marked. c. Details on the specific inlets and outlets and direction of convective (vertical arrows) and diffusive (horizontal block arrows) transport.

operations [4], as well as on the effect of controlled diffusive mixing of reactants on stable gradients [9]. Microreactors were also successfully applied in fast exothermic reactions with very short residence time for the synthesis of pharmaceutical intermediates [10]. Moreover, several studies were focused on flow maldistribution in microreactors to design proper configurations that enhance the overall performance [11]. Other authors discussed mixing as a function of microchannels types, also from the perspective of pressure drops [12]. Padoin and co-authors focused on flow patterns in microchannels to assess expected flow morphology [13], while others investigated the topic of mass and heat transfer in microscale geometries [14] with a special focus on main phenomena that occur in Taylor flow regime in mini- and microchannels in multiphase systems [15].

Together with the recent fabrication technology advances, theoretical investigations and numerical simulations became crucial to predict the effects of variations in key operative parameters and to provide both design guidelines under a given set of constraints, and identify performance limitations of a given microfluidic system [16,17]. A careful modeling-based design optimization also enables a faster and better understanding of the experimental findings [18] while avoiding the costly and time-consuming trial and error fabrication steps [19,20].

Different approaches can be adopted, including Molecular Dynamics (MD), Direct Monte Carlo Simulations (DSMC), Dissipative Particle Dynamics (DPD), Continuum Method (CM), and Computational Fluid Dynamics (CFD) [21]. Among these approaches, CFD tools combine several advantages that facilitate a detailed investigation of microscale phenomena in systems characterized by low Reynolds number and/or Stokes flow, with dominant diffusion-driven mixing [18,22]. Different studies on the application of CFD to the optimization of the design of microreactors can be found in the literature, but are mostly focused on microreactors for chemical synthesis, solid-gas phase catalytic reactions, and multiphase systems. For example, Gavrilidis discussed the technology driven by optimization criteria of microengineered reactors and relevant mass and heat transfer phenomena [23]. Details on hydrodynamics and mass transfer mechanisms with CFD applicative examples can also be found [15,24,25]. A similar approach to heterogeneous reactions was proposed by Patil [26], and based on a CFD-assisted analysis of thermal gradients in a microreactor for steam-reforming. Bettermann proposed a digital and lean development method for 3D-printed reactors based on a coupled CAD modeling and CFD simulation [27]. An approach based on CFD is discussed by Mbodji and coworkers, investigating heat and external mass transfers in a channel geometry made of coated catalytic walls [28]. Recently, a study addressed the phenomenon of droplet-based flow in poly(dimethylsiloxane) (PDMS) devices [29].

Nevertheless, the investigation on these topics for biologically targeted applications is still limited, and systematic practical guidelines for microfluidic devices and reactors that operate with living, cell-based samples are still missing.

We here discuss and propose a systematic optimization of microfluidic gradient generators through numerical simulations, presenting guidelines and design specifications amenable to adaptation to different experimental needs. We finally present a case study, resulting from the synergy between modeling, design, manufacturing, and validation. Our device enables repeatable and reliable high throughput experiments and was optimized to perform screen studies on biological samples such as exposure to drug concentration gradients for antibiotic susceptibility tests or therapy development.

Table 1
Key MGG design parameters and their main effects.

Building block	Key parameters	Effects and governed phenomena
SoBB, SiBB (feeds)	Geometry: width and height, shape; Inlet flow rate; Inlet concentration	Average velocity, velocity distribution in space and time, flow regime
DBB (microfluidic channels)	Geometry: hydraulic diameter, length; Spatial arrangement; Number of channels	Pressure drops, flow regime, mass transfer regime, entry length
TBB(culture chamber)	Volume; Geometry: width and height, shape	Diffusion characteristic time, mixing, manufacturing, cell viability

2. Materials and methods

2.1. General geometry of microfluidic gradients generators (MGGs) and implications

MGGs are experimental tools providing stable concentration gradients in space and time, an essential feature to accurately study biological systems reproducing physiologically sound microenvironments matching the characteristic time and space scales of biological phenomena [30]. A successful geometric and fluid dynamics parameter coupling not only ensures an accurate performance and control over the culture microenvironment, but also provides conditions for the establishment of a steady-state, essential to ensure maintenance of constant levels of the specific species of interest.

From a general perspective, a MGG can be represented as a basic 5-building blocks system (Fig. 1) with axial symmetry. The source and sink building blocks (SoBB and SiBB, respectively) drive the culture medium inlet feeds; the SoBB typically delivers media added with a species of interest, while the SiBB is depleted in the same species. The delivery building blocks (DBBs), systems of microfluidic channels, link the source and sink to the target building block (TBB), which is the culture chamber where cells will be seeded. These building blocks are physically and geometrically connected, and the arrows in Fig. 1a represent the dominant directionality of fluxes: convective transport follows perfusing streams entering from the SoBB and SiBB top inlets and exiting from the bottom ones, while diffusion is mainly perpendicular with a source-to-sink direction. Schematics of the proposed device are also given in Fig. 1b and c, introducing the key geometrical parameters and locations of all inlets and outlets for fluid perfusion and cell seeding.

Each constitutive block is characterized by a set of physical and geometric parameters ultimately determining the shape of the gradient inside the TBB and the time-to-steady-state. The key parameters for each block and their main effects are listed in Table 1.

All geometric constraints are tied to both operational requirements and manufacturing limitations (i.e. the microfluidic channels must be within defined aspect ratios to ensure structural stability while ensuring the desired flow and transport regime). The key geometrical feature for the SoBB and SiBB is their width that, according to the imposed inflow of culture medium, determines the dominant flow regime. When a laminar flow is established, viscous forces dominate over convective transport and controlled molecular diffusion ensures the formation of a stable and predictable concentration profile in the TBB. Other operational parameters are the culture medium inlet flow rate and the species concentration, all imposed as system boundary conditions. Mass and momentum are transferred from the SoBB and SiBB to the TBB across the delivery building block DBB; microchannels should thus be designed to minimize convective contributions to transport phenomena. Considering the intended biological application, the main determinants of the dimensions of the TBB, the cell culture chamber, are its volume and shape. The volume will establish the quantity of culture media available to cells, and the surface area the total number of cells. Nutrients and reactants are distributed in space and time across the DBB, designed to operate as a pressure drop generator where induced shear stresses and velocity gradients determine the reduction of convective contributions. Geometry, number, and arrangement of the microchannels are key parameters that determine the success in realizing a stable diffusive gradient. Each channel of the network contributes to the overall pressure drops ΔP_{tot}; as a rule, pressure drops scale according to $\sim < v > L d_{eq}^{-2}$, where $< v >$ is the mean laminar flow velocity, L the microchannel length and d_{eq} the equivalent hydraulic diameter. While the mean velocity is controlled by operative conditions in the SoBB and SiBB, the geometric constraint on d_{eq} and L depends on both manufacturing limitations and time-to-gradient-establishment (see Section 3).

2.2. FEM numerical simulation of micro-gradient generators

Numerical modeling applied to MGG design plays a crucial role in investigating fluid dynamics and mass transport phenomena. We here describe our Comsol Multiphysics®-based CFD modeling approach to shed light on detailed features that cannot be easily experimentally screened given the time- and resource-demanding processes for the production of microscale platforms [18].

2.2.1. Constitutive equations and phenomena

Numerical simulations are based on the detailed description of physical domains through discretization and solution of mathematical equations in a finite number of points of the domain (*mesh*). The solution region is discretized in small sub-regions (typically triangular and quadrilaterals) where linearized or non-linearized equations are solved simultaneously. The Finite Element Method (FEM) approach is intended as an example of the discretization procedure of problems in continuous domains [31,32]. Solving procedures typically involve the following steps: discretization, selection of interpolation functions, formulation, mathematical system assembling, and solving.

The investigation of the performance of a MGG requires the simultaneous analysis of two physical phenomena: fluid dynamics and mass transfer. Since living cells are typically kept at 37 °C inside culture incubators, the system is treated as an isothermal domain and energy balances can be discarded [33]. The small characteristic lengths in microfluidic systems enable the application of the laws for laminar flow in closed conduits (in most cases $Re < 100$), with negligible inertial forces, mixing determined by diffusional mechanisms and, overall, simplification of the mathematical models[16,30,34]. Mass transport inside an isothermal MGG is related to convection and diffusion through the dimensionless Péclet number ($Pe = Re{\cdot}Sc$,[35]). Microscale systems typically operate at low Pe numbers (ideally $Pe \ll 1$), where diffusive mass transport becomes dominant over convection enabling the establishment of complex and controlled concentration gradients [36]. In this scenario, an effective mixing should maximize the action of diffusion without significant increases in the time required for gradient stabilization [37].

On this basis, the equations to be solved are the Navier–Stokes for the conservation of momentum Eq. (1), and the continuity equation for the conservation of mass Eq. (2):

$$\frac{\partial \rho \boldsymbol{u}}{\partial t} + \nabla \bullet (\rho \boldsymbol{u}) = 0 \tag{1}$$

$$\frac{\partial \rho \boldsymbol{u}}{\partial t} + \nabla \bullet (\rho \boldsymbol{u}\boldsymbol{u}) = -\nabla P + \nabla \bullet \tau + \boldsymbol{F} \tag{2}$$

where ρ is the density, $\boldsymbol{u}$ the velocity vector, P the pressure, τ the viscous stress tensor, $\boldsymbol{F}$ is the vector of forces.

Concentrations at play justify the adoption of the built-in module for the transport of diluted species in solvent (culture media). In the presence of both diffusion (described by Fick's law) and convection, the combined mass balance equation for the transported species of choice is solved (Eq. (3)):

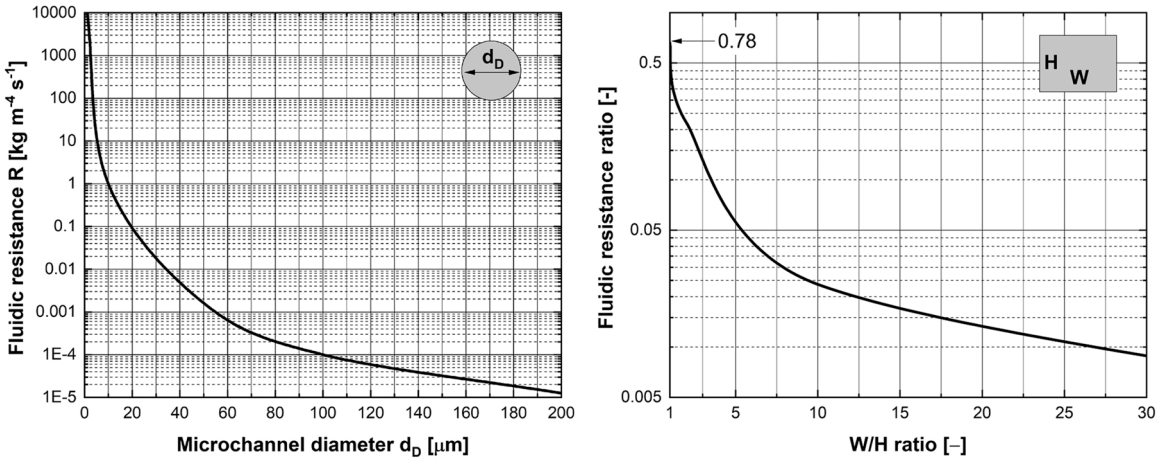

Fig. 2. Fluidic resistances in circular and rectangular microchannels. Values of R for a single channel are plotted: for circular channels as a function of the internal diameter d_D (left); and for rectangular channels as the ratio with the reference fluidic resistance of a circular channel with internal diameter d = H.

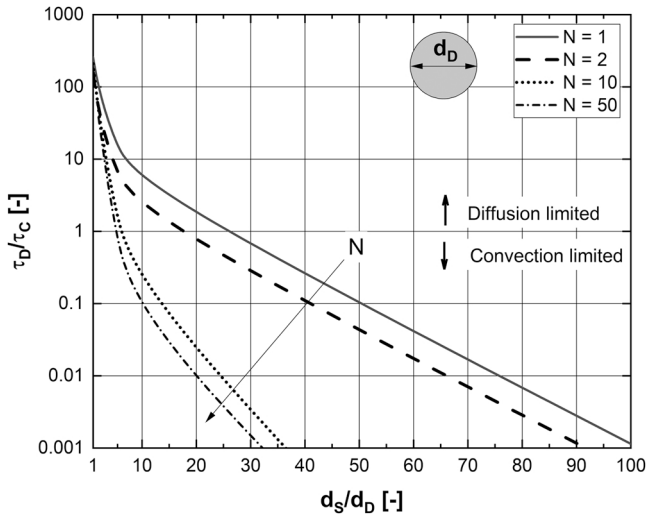

Fig. 3. $\frac{\tau_D}{\tau_C}$ analysis for circular microchannels. Curves represent average $\frac{\tau_D}{\tau_C}$ values inside the TBB with fixed inlet medium flow rate, feed channel diameter d_s and TBB geometry. Curves are parametric in the total number N of parallel microchannels with diameter d_d forming the DBB.

$$\frac{\partial c_i}{\partial t} + \nabla \bullet (-D\nabla c_i) + u \bullet \nabla c_i = 0 \tag{3}$$

where c_i is the concentration of a solute i, D is its diffusion coefficient and u is the local velocity vector. The concentration field $c_i(x,t)$ expected in the culture chamber, and governed by the parameters discussed in 2.1, is key for the proper design of a MGG. It was assumed that the flowing fluid had the same characteristic as water at 293.15 K with constant dynamic viscosity, given the negligible solute amount used in the experiments.

2.2.2. Initial (IC) and boundary conditions (BC)

Eq. (4) was solved in a 3D space under laminar flow conditions, with the FEM approach allowing for the calculation of the local velocity field u once initial (ICs) and boundary conditions (BCs) are imposed. IC simulated an empty MGG at $t = 0s$ (Eq. (4)), and BCs were defined as time-invariant. The inlet BC for the flow phenomena was imposed as a constant mass flow rate (Eq. (5)), coupled with an outlet BC of pressure without stress condition, restricting the solver to maintain the pressure at a given value p_o (i.e. zero relative pressure). No-slip BCs (zero velocity) were imposed at all internal walls (Eq. (7)). For mass transport, a solute concentration C_0 was specified in combination with inflow conditions (Eq. (8)), while the outflow was imposed to ignore diffusive transport across the outlet border (Eq. (9)). Concentration values are

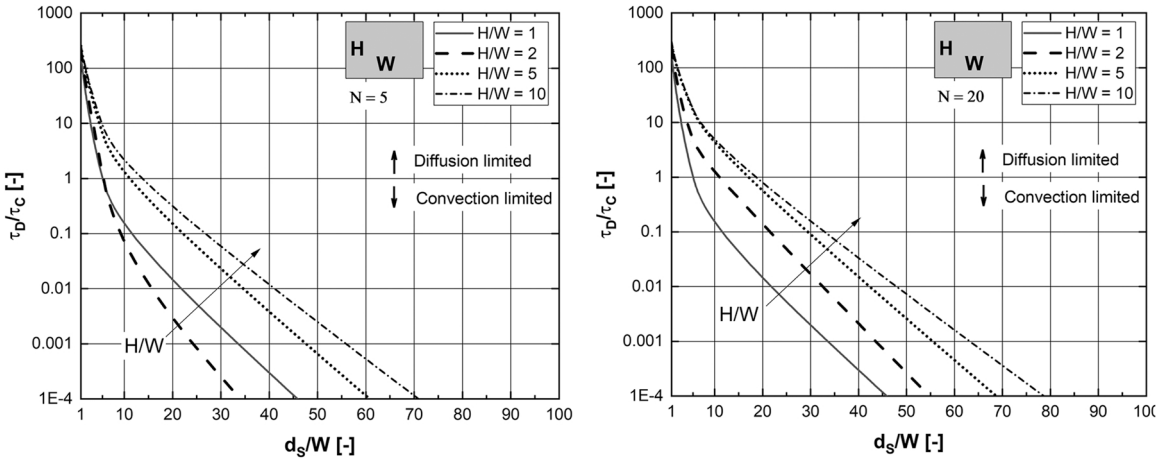

Fig. 4. $\frac{\tau_D}{\tau_C}$ analysis for rectangular microchannels. Curves represent average $\frac{\tau_D}{\tau_C}$ values inside the TBB with fixed inlet medium flow rate, feed channel diameter d_s and TBB geometry. Curves are parametric in the geometric ratio H/W (height/width) of rectangular microchannels. Left plot: the number of channels is $N = 5$; right plot: $N = 20$.

Table 2
Main characteristics of the modeled MGGs. W is the relevant width, H the height, L the length, A the surface area, and V the volume. Superscripts and subscripts specify the BB and the x-y orientation, as highlighted by annotations in the schematics of the last column.

Building Block	Geometrical Feature	A	B	C
SoBB	W_{Sx} [mm]	2.00	2.00	1.00
SiBB	H [mm]	0.12	0.12	0.12
	L_{Sy} [mm]	18.20	16.00	14.00
	W_{Dx} [mm]	0.20	0.15	0.25
	H [mm]	0.12	0.01	0.03
DBB	L_{Dx} [mm]	5.00	5.00	2.50
	N [-]	26	34	20
	W_{Tx} [mm]	5.60	5.60	4.00
	H [mm]	0.12	0.12	0.12
TBB	L_{Ty} [mm]	11.80	10.00	10.00
	A [mm^2]	66.08	56.00	40.00
	V [uL]	7.92	6.72	4.80

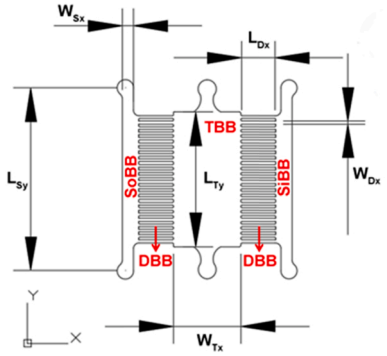

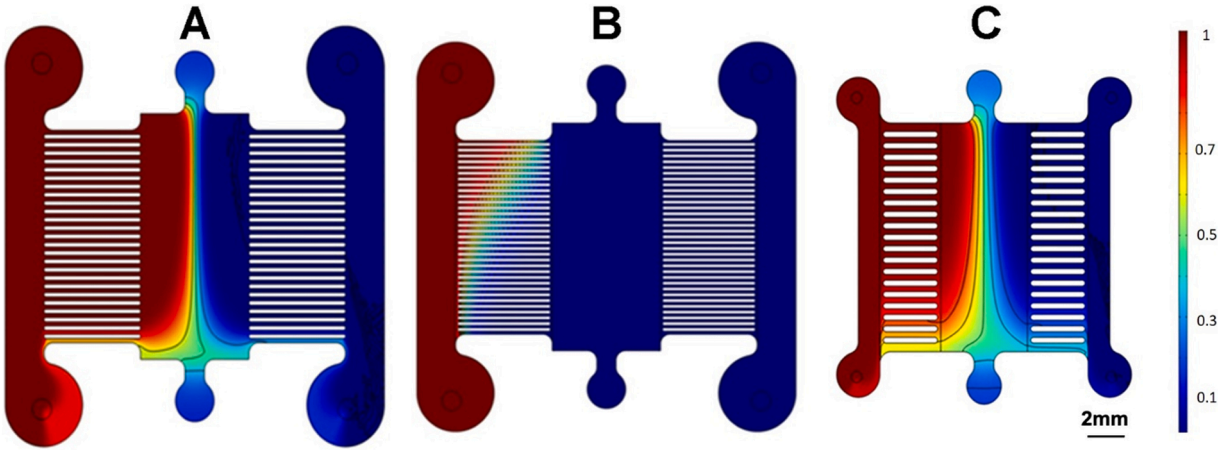

Fig. 5.. Concentration heatmaps in the modeled MGGs. Expected gradient after 1 h since initiation of perfusion at a constant flow rate of 5 µl/min for the modeled set of devices (A, B, and C) with varying characteristics for the SoBB, SiBB, and DBB. The color-coded scale bar gives normalized concentration C/C_0 *values.*

typically represented as normalized by the IC of C_0.

Initial and boundary conditions are listed below:

$$\boldsymbol{u}(t=0)=0 \tag{4}$$

$$-\int_{\delta\Omega}\rho(\boldsymbol{u}\bullet\boldsymbol{n})ldS=\dot{m}_{in} \tag{5}$$

$$[-p\boldsymbol{I}+\boldsymbol{K}]\boldsymbol{n}=-p_o\boldsymbol{n} \tag{6}$$

$$\boldsymbol{u}=0 \tag{7}$$

$$\omega=\omega_0 \quad , \quad \omega_0=\frac{C_0M}{\rho} \tag{8}$$

$$-\boldsymbol{n}\bullet\rho D\nabla\omega=0 \tag{9}$$

where, l is the channel thickness, $\dot{m}_{in}$ the inlet mass flow rate, M the molecular weight, D the diffusion coefficient.

2.2.3. *Meshing and numerical solver*

The domain was meshed according to basic modeled phenomena and numerical requirements; discretization was based on unstructured meshes with up to 500,000 elements. A number of mesh elements and grid arrangements were selected to avoid numerical instabilities and ensure the desired degree of detail. Combinations of prismatic and tetrahedral blocks filled the simulation domain and special quadrilateral, and prismatic meshing were built close to the MGG walls and near critical points. Inaccuracies originated from the discretized approach were avoided by ad hoc mesh-sensitivity studies to get grid-independent and correct computational results.

A 3D transient model using a pressure-based solver with variable time steps was employed. In all simulations, a numerical scheme with an order of accuracy 2 was consistently adopted together with a

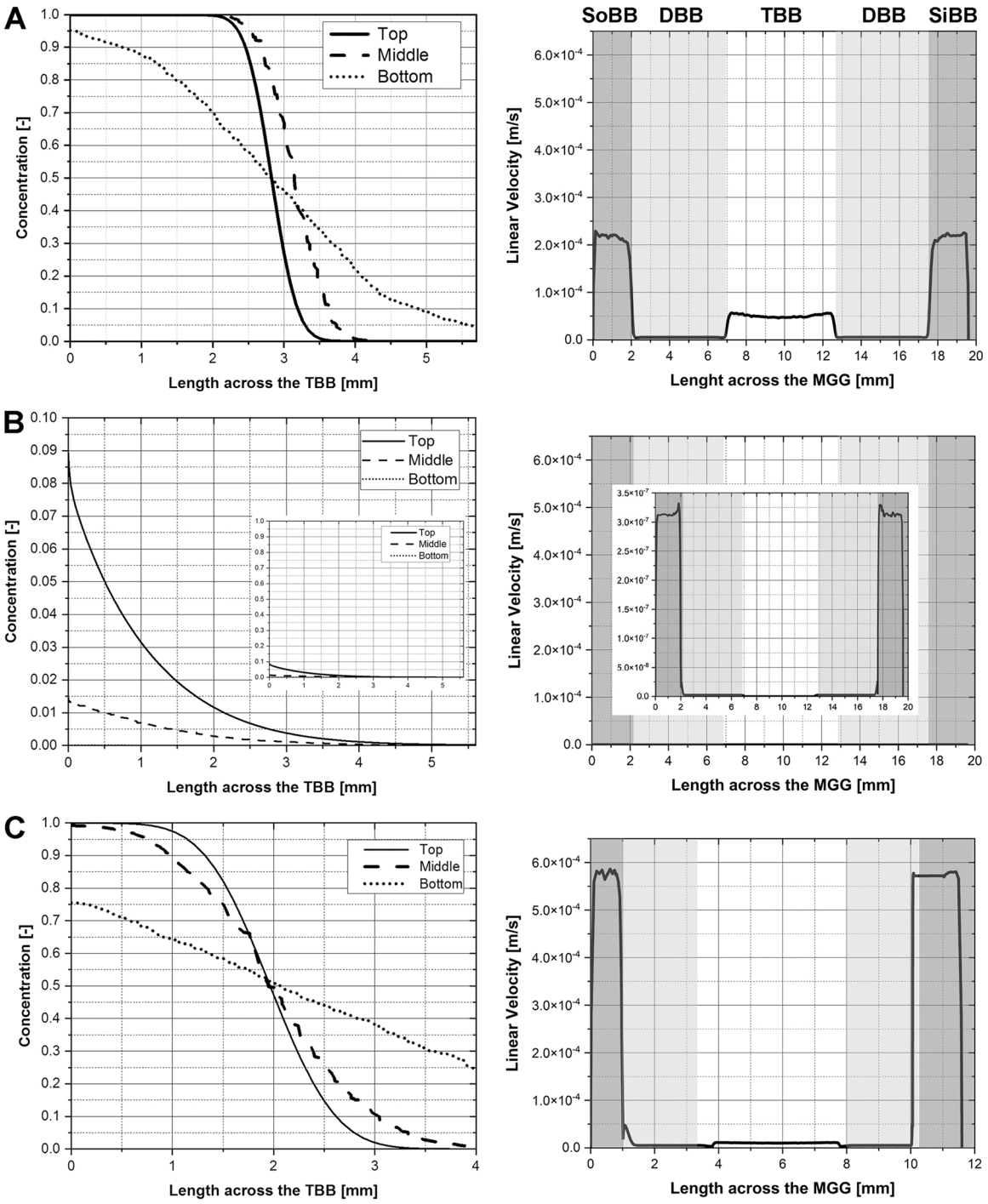

Fig. 6.. Concentration profiles in the TBB and velocity profiles for the modeled MGGs. All graphs report values obtained after 1 h since initiation of perfusion at a constant flow rate of 5 µl/min. The curves on the left panels plot normalized concentrations (C/C_0) along representative sections of the culture chamber. Inset in panel B reports the curves in the entire 0–1 range for C/C_0. On the right, velocity profiles along the horizontal mid-section of the entire MGG; shaded areas correspond to each BB, with labels specified in the top plot. Inset in panel B reports a zoomed imaged of the velocity profile.

preconditioning scheme to avoid undesired solving issues. The order of magnitude of the time step was in the range 10^{-3}-10^{-2} s to ensure Courant-Freidrichs-Leewy (CFL) condition CFL< 1 and directly managed by the numerical solver [38].

2.3. Fabrication and validation of the MGG

The microfluidic platform was produced by replica molding from an aluminum master. The master was fabricated by micro-milling an aluminum block (Kugler MICROMASTER® 5X) based on the chosen design digitalized using 3D-CAD software. Polydimethylsiloxane (PDMS) replicas of the MGG were obtained using standard techniques [39]. Briefly, PDMS was prepared by mixing the base and the curing agent in a 10:1 w/w ratio, degassed, and cast on the aluminum master. After an additional degassing step, the mold was baked in a convection oven for 75 min at 65 °C. After cooling, the PDMS was carefully peeled from the master, and the inlets, outlets, and seeding doors cored using stainless steel biopsy punches (1 mm diameter). The device was

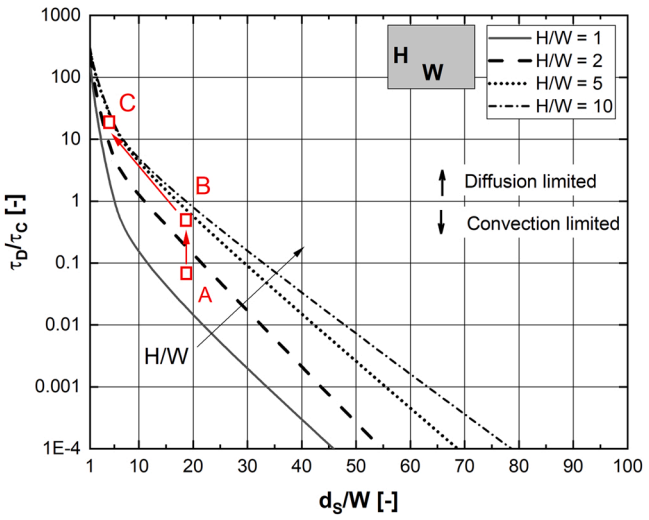

Fig. 7. $\frac{\tau_D}{\tau_C}$ analysis for the MGGs simulated. Progression of the ratio $\frac{\tau_D}{\tau_C}$ based on the simulated microdevices reported in Fig. 5. The detailed parameters of configurations A, B, and C are given in Table 2. Concentration profiles, instead, are given in Fig. 6.

irreversibly bound to a glass slide by air-plasma treatment (Harrick Plasma). The assembled unit was connected via Tygon tubing to a syringe pump (PHD Ultra, Harvard Apparatus) controlling fluid flow rates dictated by the results of the fluid dynamic modeling.

The assembled MGGs was validated with dyes, using different color combinations for the inlets and following the formation of the concentration gradient inside the TBB. Images were acquired using a digital camera at a specified magnification and at different time points: 30 min, 8, and 24 h. Pictures were captured focusing on the cell culture chamber. Additional validation was performed using fluorescent dextran as a tracer (Isothiocyanate-dextran, Sigma-Aldrich, St. Louis, MO, USA) dissolved in DI water at a concentration of 0.5 mg/10 mL. Images at different time points were acquired using a fluorescent microscope (EVOS Floid Imaging System) at 4x magnification, allowing to reconstruct the entire culture chamber. Image analysis was performed using ImageJ. Briefly, images were converted in 16-bit, the average fluorescence intensity in selected areas was quantified, correlated to the concentration profiles, and plotted along the TBB.

2.4. Cell culture

Human embryonic kidney cells (HEK-293 T) were used to study the biocompatibility of the assembled platform. Cells were maintained in culture in 75 cm^2 flasks in Dulbecco's Modified Eagle Medium (DMEM) supplemented with 10% of fetal bovine serum, 1% of glutamine, and 1% of antibiotics (Penicillin/Streptomycin). Before cell seeding, the MGG was autoclaved (121 °C for 35 min) and then the surface of the TBB was coated with 25 μg/mL Fibronectin (Thermo Fisher Scientific) for 1 h at room temperature. The cells were seeded at a density of 1000cells/mm^2 and cultured for 24 h in static conditions. For biocompatibility studies, cells were stained with a Posphate Buffer Saline (PBS) solution of Hoechst marking all nuclei in blue (1:1000 dilution, Sigma-Aldrich, St. Louis, MO, USA), Calcein-AM marking the cytoplasm of living cells in green (1:1000, Sigma-Aldrich, St. Louis, MO, USA), and Propidium Iodide marking dead cells nuclei in red (1:500, Sigma-Aldrich, St. Louis, MO, USA) for 30 min. Images were acquired on a fluorescence microscope (EVOS Flois Imaging System) and analyzed with the "Analyze particles" tool of ImageJ software. Automated cell counting enabled the quantification of living cells over the total number of cells, as a measure of cell viability. Cell counting was repeated on at least 10 images.

3. Modeling, sizing guidelines, and case study

This section will present our computational results and describe the general features of the proposed MGGs. The results have general validity and were here used to guide the parameter selection for a representative case study MGG.

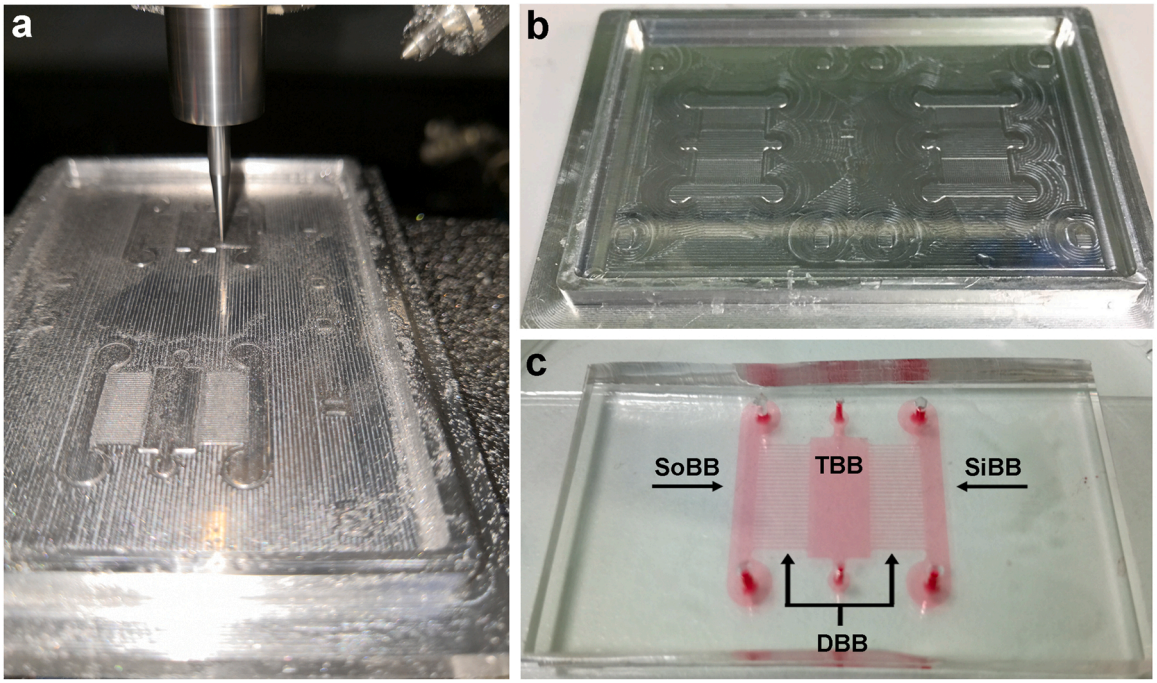

Fig. 8.. Fabricated MGG. a. Aluminum mold during the micro-milling process and b. after cleaning. c. Replica of the MGG irreversibly attached to a glass slide after plasma treatment. A dye is used to fill the device and ease visualization of the building blocks showing details of each geometrical feature. All building blocks are marked.

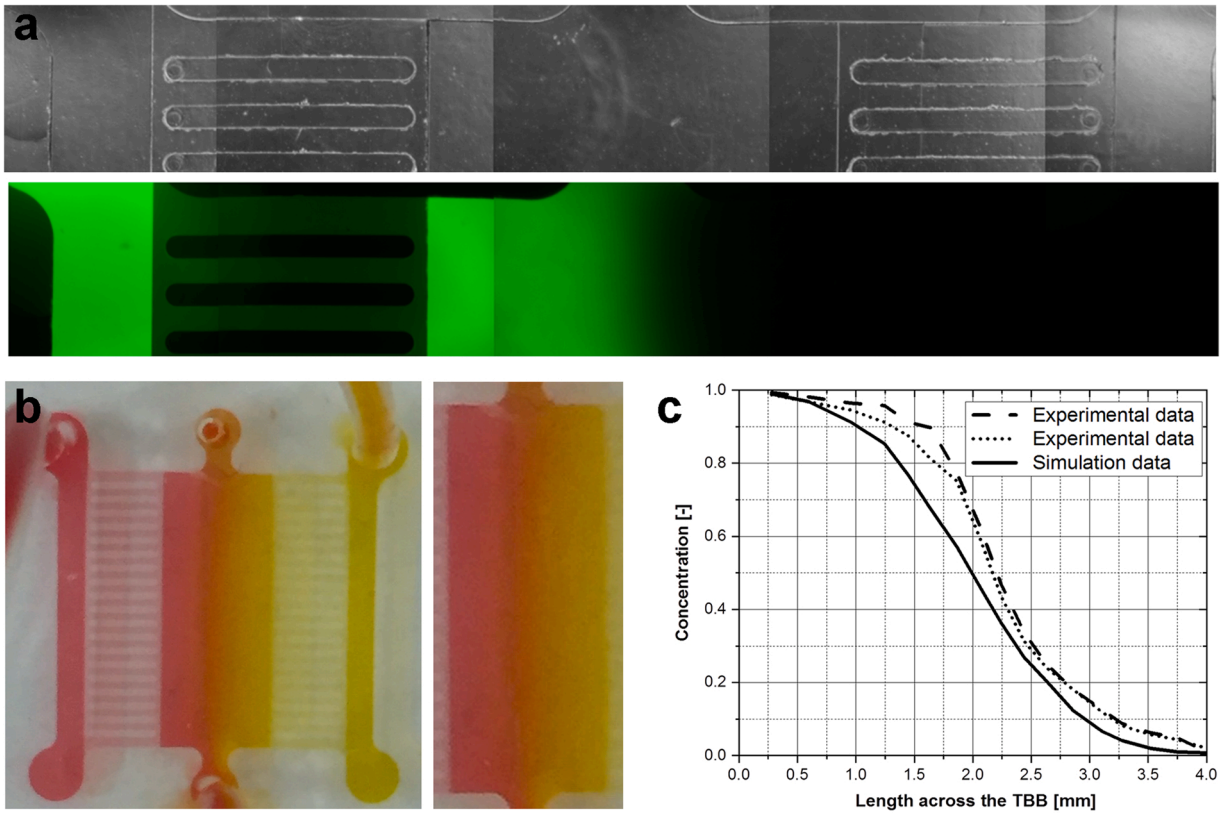

Fig. 9.. Fluid-dynamic validation of the MGG. a. Bright field (top) and fluorescence (bottom) images reconstructing the entire section of the TBB. Perfusion rate was set at 5 μl/min and pictures were taken after 30 min. A solution of green fluorescent dextran in DI was injected from the SoBB (left channel) and pure DI from the SiBB (right channel). b. Image of the entire MGG and a zoomed view of the TBB at the same perfusion conditions used for panel a. obtained flowing colored dyes (red from the SoBB, and yellow from the SiBB). c. Concentration profiles obtained from the semi-quantitative image analysis on fluorescent gradients obtained as in panel a. Data represent normalized fluorescence intensity across a section of the TBB. The solid curve represents the concentration profile obtained through Comsol Multiphysics Simulation.

3.1. Sizing guidelines

The core of a MGG is the DBB: besides posing the biggest challenges in terms of fabrication, its configuration is the main player in determining the capability of the device to sustain a specified gradient inside the TBB and the time-to-steady state. The number, layout, and geometry of its microchannels are key variables that can be manipulated. The combination of geometric and operative parameters for the DBB determine the fluidic microchannels resistance R_{tot} and the average flow rate $Q = \Delta P_{tot}/R_{tot}$. Manufacturing solutions could include both circular and rectangular microchannels geometries with corresponding channel resistance R_i under laminar flow given by Eqs. (10–11) [40], respectively:

$$R_{i,c} = \frac{8\mu L}{\pi\left(\frac{d_D}{2}\right)^4} \tag{10}$$

$$R_{i,r} = \frac{12\mu L}{WH^3}\left[1 - \frac{H}{W}\left(\frac{192}{\pi^5}\sum_{n=1,3,5}^{\infty}\frac{1}{n^5}tanh\left(\frac{n\pi W}{2H}\right)\right)\right]^{-1} \tag{11}$$

Eq. (11) refers to a rectangular microchannel with width W and height H. μ is the fluid dynamic viscosity, L is the microchannel length. The hydraulic diameter of rectangular microchannels is calculated according to the definition $d_{eq} = \frac{2WH}{(W+H)}$. The resistance of a rectangular duct under laminar flow with a high aspect ratio, i.e. $W \ll H$ or $H \ll W$, is approximately given by $R_{i,r} \approx (12\mu L)/(WH^3)$.

Fluidic resistances of circular and rectangular microchannels are reported in Fig. 2.

Another key geometric parameter for the DBB is the microchannel length, determining the hydrodynamic entry length L_e ensuring the establishment of a fully developed flow [41], in turn required to sustain a stable flow feeding the TBB where cells are cultured. Given the laminar flow field, L_e depends on the equivalent diameter d_{eq} and the duct geometry. For circular channels L_e varies almost linearly with $Re \bullet d$ [42] and a similar correlation can be found for rectangular ducts [43]. Since microdevices usually operate at $Re < 100$, L_e is generally < 25 μm. Microchannels with $L \gg L_e$ dilate transients and reduce the system response to input variations [30], slowing the effect of diffusion and the establishment of the desired concentration field. A minimal overdesign margin is always considered to accommodate constraints related to the manufacturing procedure of choice [44]. In addition, since the device is typically replica-molded using Polydimethylsiloxane (PDMS), to ensure structural stability and geometrical uniformity throughout the entire set of microchannels, features must have a width-to-height ratio greater than 1:10 and smaller than 10:1.

The microchannel network induces both distributed pressure drops and localized flow dissipations (i.e. junctions, piping connections, flow contractions/expansions, …). Localized losses are proportional to the network complexity, and the overall resistance $R_{tot,n}$ can be calculated considering a parallel arrangement of N channels as of Eq. (12):

$$R_{tot,n} = \frac{1}{\sum_{i=1}^{N}\left(\frac{1}{R^i_{tot,d}} + \frac{1}{R^i_{tot,c-in}+R^i_{tot,c-out}}\right)} \tag{12}$$

Each channel contributes with a resistance related to distributed pressure drops $R^i_{tot,d}$ as of Eq. (10−11), and localized losses mainly ascribable to the piping inlet (contraction) $R^i_{tot,c-in}$ and outlet (expansion)

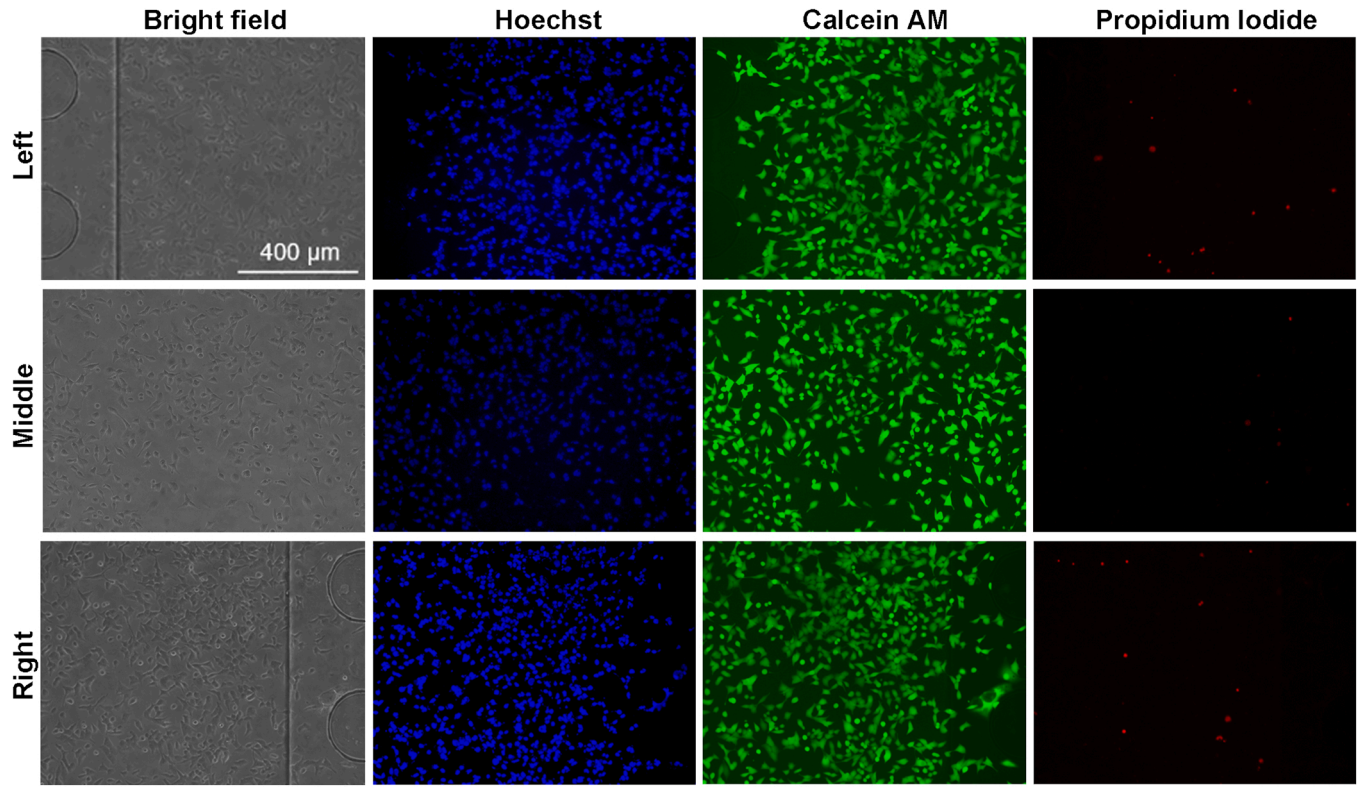

Fig. 10.. Cells viability after MGG culture. HEK-293 T were cultured for 24 h in the TBB of the MGG in static conditions. Bright-field images show the connection between the DBB and the TBB. Hoechst marks all cell nuclei in blue, while Calcein AM marks the cytoplasm of live cells in green. Finally, Propidium Iodide stains nuclei of cells in the final stage of apoptosis in red. From top to bottom, the rows of images are representative of a section: close to the left DBB, at the center of the TBB, and close to the right DBB.

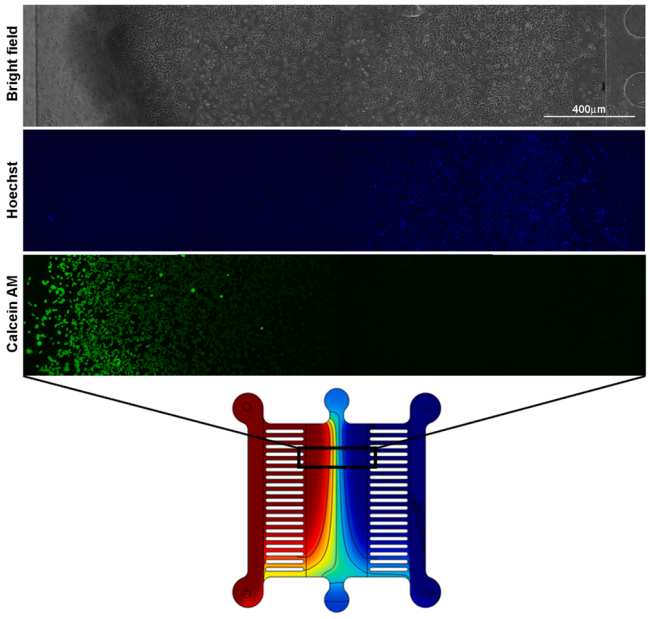

Fig. 11.. Cells exposure to a double concentration gradient. Images reconstruct an entire cross-section of the TBB after 24 h of exposure to the concentration gradient. The concentration of the fluorescent markers varies as follows: Calcein-AM (green) has a maximum towards the left inlet and is zero at the right; Hoechst (blue) is symmetric, with a maximum on the right and zero on the left. The experimental evidence correctly mirrors the results of the CFD simulation reported in the bottom panel as a reference.

$R^i_{tot,c-out}$. The contribution related to concentrated pressure drops is increased with the complexity and number of elements that compose the DBB. Similarly, the concentration field in the TBB is affected by an increased time for stabilization and higher pressure drops.

We now understand how the DDB configuration is the main determinant of the device capability to sustain a specified gradient inside the target TBB, but its fast establishment and stability also depends on the geometric configuration of the culture chamber itself and by the convective and diffusive mechanisms with their associated time and length scales [30]. The choice of the key parameters for the TBB is mainly determined by biological requirements (sufficient number of cells and volume ensuring correct nutrients availability) and manufacturing constraints. In addition, the desired concentration profile and the time required for establishing the required profile in the TBB are sensitive to such key parameters.

The ratio between the time scale of diffusive $\tau_D = \frac{W_{Tx}^2}{D}$ and convective processes $\tau_C = \frac{W_{Tx}L_{Ty}\mathrm{H}}{Q}$ is an important indicator of the dominant transport regime inside a MGG [30]. This ratio depends on the diffusive properties of the chemical species (D is the diffusion coefficient), the TBB geometry (W_{Tx} and H are respectively the relevant width and height of the TBB), and the flow rate (Q). A ratio $\frac{\tau_D}{\tau_C} > 1$ is related to diffusion-controlled conditions, $\frac{\tau_D}{\tau_C} < 1$ is representative of processes that are convection-limited, and $\tau_D \sim \tau_C$ indicates competition between the two mechanisms. Crossing from a diffusion- to convection-limited regime can be tuned acting on the operational and geometrical parameters according to the system's degrees of freedom. If we were to fix the medium inlet flow rate and the SoBB geometry with its feed channel hydraulic diameter d_s (and the symmetric SiBB counterpart), changes in the size and number of microchannels in the DBB would affect the $\frac{\tau_D}{\tau_C}$ ratio inside the culture chamber. Plots of the $\frac{\tau_D}{\tau_C}$ profiles in the TBB when

the DBB is composed of N circular microchannels with a diameter d_D are shown in Fig. 3, and by N rectangular microchannels with aspect ratio H/W in Fig. 4. Fig. 3 shows that for $N \geq 10$ circular channels, a threshold geometric constraint $\frac{d_S}{d_D} > \sim 6$ is required to cross from a diffusion- to a convection-controlled regime inside the culture chamber.

The generalized curves presented in Fig. 3, and 4 can thus be used as guidelines for the design of a DBB determining the desired $\frac{\tau_D}{\tau_C}$ ratio inside the TBB.

In a biological setting, different solutes with sizes spanning several orders of magnitudes can be added to culture media and used in a MGGs. According to the definition, the solute's diffusion coefficient contributes to determining the time scale for diffusion. Greater molecular weights will decrease the diffusion coefficient, increasing the associated time scale. For example, a molecular size of 10 kDa corresponds to a diffusion coefficient on the order of 10^{-11}-10^{-10} m^2 s^{-1}, one order of magnitude higher of slower-diffusing 70 kDa molecules. In summary, for a given geometrical configuration of a MGG, the behavior in the TBB may evolve from a convection- to a diffusion-limited regime for molecules with increasing molecular weights.

Based on the above-listed guidelines proving that the geometry and numerosity of microchannels shift the MGG from a convection to a diffusion-limited regime, we modeled a set of devices (A, B, and C) with varying characteristics for the SoBB, SiBB, and DBB to obtain an ideal gradient. Table 2 lists the main geometrical specifications, chosen respecting constraints derived from fabrication (minimal dimensions obtainable through micro-milling), biological (volume and surface area of the TBB), and transport (highlight regime shifts) standpoints.

In our study, we screened a simulated range of inlet flowrates from 0.1 to 100 μl/min (Supplementary Fig. S1). Fig. 5 shows the simulated gradients as normalized concentration heatmaps (C/C_0) at $t = 1\ h$ after initiation of perfusion where we fixed: *i.* the inlet flowrate (5 μl/min), *ii.* the fluid density (998 kg/m^3) and *iii.* viscosity ($8.9 \cdot 10^{-4}$ Pa·s). The inlet flow rate of 5 μl/min was chosen since it resulted in the fast establishment of a stable concentration gradient inside the culture chamber (within 1 h) with low shear forces.

Fig. 6, left column, further analyzes the concentration profiles in the TBB for the modeled configurations by plotting normalized values along 3 representative sections: *i.* top, located between the 1st and 2nd microchannel; *ii.* middle, located at the middle of the TBB, and *iii.* bottom, located between the last and 2nd to the last microchannel. Plots on the right report also the modeled plug-flow velocity profiles along the horizontal mid-section of the entire MGG for the same configurations (A, B and C).

Finally, Fig. 7 locates the operating range of each modeled configuration (A, B, and C) in terms of the $\frac{\tau_D}{\tau_C}$ ratio superimposed to the curves obtained with the calculations for the case of N = 20 microchannels (as in Fig. 4, right plot). This further highlights how key parameter modifications in the SoBB/SiBB and DBB shift the transport regime from convection- to a diffusion-dominated regime in the TBB. As of Fig. 7, the condition $\frac{\tau_D}{\tau_C} > 1$, which consists of a diffusion-limited regime in the TBB (culture chamber), is always satisfied once rectangular microchannels are manufactured according to $d_S/W < 10$ and $H/W > 2$.

Taken together, the results presented in Figs. 5-7 prove how key features of the MGG affect the characteristics of the concentration gradient formed in the TBB. Each of the three designed and fabricated configurations generated a specific concentration field in the TBB. Although both A and C resulted in an appropriate concentration field in the TBB within 1 h since initiation of perfusion at a constant flow rate of 5 μl/min, configuration C was preferred for its intended application. C optimized both concentration and velocity profiles: concentration profiles were smoother than those generated by A, thus enabling to expose more cells to different concentration levels; velocity profiles in the culture chamber were flat and uniform, their low values also ensured that the developed shear stresses wouldn't be harmful to the cultured cells.

Based on our biological target application and experimental requirements such as time-to-steady-state (<1 h), stability, symmetry, and shape, the optimized microfluidic device is represented by case C. However, all modeled devices were produced and validated to confirm the results obtained through the fluid dynamics simulation (please see supplementary Fig. S2 for case A, and S3, S4 for case B). Briefly, our results highlight how case A refer to MGGs that are configured to precisely control time, shape, and size of fluid interfaces, allowing limited diffusive transport between the left and right compartments. This system could thus enable fine-tuning of specific interface properties. If fluids are immiscible, the interface between the two phases can act as a semi-permeable wall; if they are miscible, a "*moving interface*" generates under laminar conditions so that the boundary between the fluids moving and mixing only through diffusion can be manipulated and adapted to specific experimental needs. An additional interesting feature emerging from case B simulations is the manifestation of the *Coanda Effect* inside the microchannels (supplementary Fig. S4). In jet-like flows, the high friction at the walls determines a "sticky" behavior in the fluid streams, which attach to the surface even when curving away from the original jet direction.

3.2. Results and discussion of a case study

3.2.1. MGG fabrication

The optimized device was designed based on the modeling results and to obtain a stable concentration gradient within 1 h. To summarize, the MGG had the following geometrical features:

- SoBB and SiBB: two symmetric lateral channels, each with an inlet and an outlet used to flow fluids at different concentrations inside the platform (1.00 ×0.12 ×14.00 mm; W_{Sx}, H, and L_{Sy});
- DBB: two series of 20 rectangular microchannels (0.25 ×0.03 ×2.50 mm; W_{Dx}, H, and L_{Dx});
- TBB: a cell culture chamber equipped of two seeding doors (4.00 ×0.12 ×10.00 mm; W_{Tx}, H, and L_{Ty}).

The aluminum master and an assembled MGG are shown in Fig. 8. The aluminum master had an overall size of 50 × 75 mm, while the replica MGG was cut as a 20 × 50 mm rectangle to fit over a standard 25 × 75 mm microscope slide.

3.2.2. MGG fluid-dynamic validation

The platform was experimentally validated, and its performance compared with the fluid dynamics simulations; representative results are shown in Fig. 9. Qualitatively, images taken after 30 min since fluid flow initiation show the correct formation of a colored gradient in the cell culture area. The platform also succeeded in maintaining a steady-state gradient for at least 24 h in all tests performed. The semi-quantitative image analysis of the dextran fluorescence intensity across the width of the TBB led to the concentration profiles plotted in panel c. A comparison with the reference curve obtained from the corresponding fluid dynamics simulation (solid line) highlighted great accordance between experimental and modeled data.

3.2.3. MGG biological validation

Fig. 10 reports representative images for the three markers used in the biocompatibility validation of the device. The percentage of living HEK-293 T cells after one day inside the microfluidic device was 95.9% ± 4.3%.

HEK293-T were then seeded at the same density of the biocompatibility experiments and exposed to a double concentration gradient. In detail, 24 h after seeding the two inlets were connected through Tygon tubing to two syringes filled with DMEM solutions with Hoechst (marking cell nuclei) on one side, and Calcein-AM (marking the cytoplasm of live cells). The syringes were connected to the pump setting a constant flow rate of 5 μl/min, and the MGG was correctly placed in the

incubator. The Calcein-AM solution was connected to the SoBB (left inlet), and Hoechst to the SiBB (the right one), enabling the formation of a double left-to-right and right-to-left gradient. Given the fast establishment of the steady-state and rapid uptake of the dyes by the cells, the formation of the gradient was assessed 30 min after starting perfusion and at the 24 h time point using a fluorescent microscope (EVOS Floid Imaging System).

Images in Fig. 11 prove the correct formation of the concentration gradients in the culture chamber with fluorescent signals detected only in one-half of the chamber and with intensity reflecting the graded concentration generated by the device.

4. Conclusions

Numerical simulations are of great support in the sizing and development of microfluidic gradient generators, where desired concentration patterns can be adequately controlled. Device features and manufacturing parameters are crucial in determining a suitable stable gradient, to be generated within a proper time and under imposed experimental boundary conditions.

In this work, a conceptual systematization of microfluidic gradient generator devices was proposed as a foundation for a synergistic approach between numerical modeling and device manufacturing.

Simulations were used to optimize the size and the fluid dynamics of each device key component (lateral channels, microchannels, culture chamber) to give a stable concentration gradient within a suitable experimental timing. Sizing and manufacturing guidelines were illustrated and discussed to correlate geometric features, device performances, and the required gradient. Our guidelines, which are of general use, successfully supported the device conceptualization and development, and were validated experimentally via a case study. Results of the numerical simulations led to an optimized geometry that was fabricated using micro-milling techniques to produce the aluminum mold, and replica molding in PDMS to obtain several copies of the device. The case-study device was successfully reproduced and used for several validation experiments, first with colored tracers and then with live cells. The microfluidic platform, which design was optimized based on the results of numerical simulations, proved suitable to rapidly obtain a continuous and stable concentration gradient.

Although used to respond to specific biomedical requirements, our approach can be translationally applied to different fields spanning from applications in traditional reaction engineering systems to peculiar mixing problems and used to guide the design of development of ad hoc microreactors.

CRediT authorship contribution statement

Sara Micheli: Conceptualization, Methodology, Validation, Investigation, Writing – original draft. **Paolo Mocellin**: Conceptualization, Methodology, Software, Validation, Investigation, Writing – original draft. **Marco Sorgato**: Methodology, Validation. **Lorenzo Bova**: Methodology, Visualization. **Elisa Cimetta**: Conceptualization, Methodology, Writing – original draft, Writing – review & editing, Supervision, Funding acquisition.

Declaration of Competing Interest

The authors declare that they have no known competing financial interests or personal relationships that could have appeared to influence the work reported in this paper.

Acknowledgements

The work was supported by European Research Council Starting Grant (ERC-StG) MICRONEX (UERI17, PI E Cimetta) and by SID Department of Industrial Engineering (DII) University of Padua grant (CIME_SID16_01, PI E Cimetta).

Appendix A. Supporting information

Supplementary data associated with this article can be found in the online version at doi:10.1016/j.bej.2022.108415.

References

[1] A.G.G. Toh, Z.P. Wang, C. Yang, N.-T. Nguyen, Engineering microfluidic concentration gradient generators for biological applications, Microfluid. Nanofluid. 16 (2014) 1–18, https://doi.org/10.1007/s10404-013-1236-3.
[2] D. Qian, A. Lawal, Numerical study on gas and liquid slugs for Taylor flow in a T-junction microchannel, Chem. Eng. Sci. 61 (2006) 7609–7625, https://doi.org/10.1016/j.ces.2006.08.073.
[3] T. Zhou, T. Liu, Y. Deng, L. Chen, S. Qian, Z. Liu, Design of microfluidic channel networks with specified output flow rates using the CFD-based optimization method, Microfluid. Nanofluid. 21 (2017) 11, https://doi.org/10.1007/s10404-016-1842-y.
[4] R. Prado, E. Borges, Microbioreactors as engineering tools for bioprocess development, Braz. J. Chem. Eng. 35 (2018) 1163–1182, https://doi.org/10.1590/0104-6632.20180354s20170433.
[5] D. Friedrich, C. Please, T. Melvin, Design of novel microfluidic concentration gradient generators suitable for linear and exponential concentration ranges, Chem. Eng. J. 193–194 (2012) 296–303, https://doi.org/10.1016/j.cej.2012.04.041.
[6] H.S. Rho, A. Hanke, M. Ottens, H. Gardeniers, A microfluidic chip with a staircase pH gradient generator, a packed column and a fraction collector for chromatofocusing of proteins, Electrophoresis 39 (2018), https://doi.org/10.1002/elps.201700341.
[7] G. Vozzi, D. Mazzei, A. Tirella, federico vozzi, A. Ahluwalia, Finite element modelling and design of a concentration gradient generating bioreactor: application to biological pattern formation and toxicology, Toxicol. In Vitro 24 (2010) 1828–1837, https://doi.org/10.1016/j.tiv.2010.05.010.
[8] R. Watanabe, T. Komatsu, S. Sakamoto, Y. Urano, H. Noji, High-throughput single-molecule bioassay using micro-reactor arrays with a concentration gradient of target molecules, Lab Chip 18 (2018), https://doi.org/10.1039/C8LC00535D.
[9] T. Zhang, J. Meng, S. Li, C. Yu, J. Li, C. Wei, S. Dai, A. Microfluidic, Concentration gradient maker with tunable concentration profiles by changing feed flow rate ratios, Micromachines 11 (2020) 284, https://doi.org/10.3390/mi11030284.
[10] J.C.K. Song, H. Kwon, Microreaction technology in practice, Stud. Surf. Sci. Catal. 159 (2006).
[11] D.F. del Pozo, T. Van Daele, D. Van Hauwermeiren, K.V. Gernaey, I. Nopens, Quantifying the importance of flow maldistribution in numbered-up microreactors, Comput. Aided Chem. Eng. 38 (2016) 1225–1230, https://doi.org/10.1016/B978-0-444-63428-3.50209-5.
[12] F. Huchet, J. Comiti, P. Legentilhomme, H. Bennadji, Mixing characterization and energetic dissipation in different networks of minichannels, Chem. Eng. Res. Des. 86 (2008) 1135–1142, https://doi.org/10.1016/j.cherd.2008.04.008.
[13] N. Padoin, A.Z. de Souza, K. Ropelato, C. Soares, Numerical simulation of isothermal gas-liquid flow patterns in microchannels with varying wettability, Chem. Eng. Res. Des. 109 (2016) 698–706, https://doi.org/10.1016/j.cherd.2016.03.027.
[14] B. Xu, W. Cai, X. Liu, X. Zhang, Mass transfer behavior of liquid-liquid slug flow in circular cross-section microchannel, Chem. Eng. Res. Des. 91 (2013) 1203–1211, https://doi.org/10.1016/j.cherd.2013.01.014.
[15] S. Haase, D.Y. Murzin, T. Salmi, Review on hydrodynamics and mass transfer in minichannel wall reactors with gas–liquid Taylor flow, Chem. Eng. Res. Des. 113 (2016) 304–329, https://doi.org/10.1016/j.cherd.2016.06.017.
[16] J. Collins, Y. Tan, A.P. Lee, IMECE2003–4 1983 IMECE2003–41983 optimization of shear driven droplet generation in a microfluidic device (2016) 1–4.
[17] G.Y. Soh, G. Yeoh, V. Timchenko, Improved volume-of-fluid (VOF) model for predictions of velocity fields and droplet lengths in microchannels, Flow Meas. Instrum. 51 (2016) 105–115.
[18] T. Glatzel, C. Litterst, C. Cupelli, T. Lindemann, C. Moosmann, R. Niekrawietz, W. Streule, R. Zengerle, P. Koltay, Computational fluid dynamics (CFD) software tools for microfluidic applications – a case study, Comput. Fluids 37 (2008) 218–235, https://doi.org/10.1016/j.compfluid.2007.07.014.
[19] N.B. Chien, N.X. Linh, O. Jong-Taek, Numerical optimization of flow distribution inside inlet header of heat exchanger, Energy Procedia 158 (2019) 5488–5493, https://doi.org/10.1016/j.egypro.2019.01.597.
[20] R. Gupta, D.F. Fletcher, B.S. Haynes, On the CFD modelling of Taylor flow in microchannels, Chem. Eng. Sci. 64 (2009) 2941–2950, https://doi.org/10.1016/j.ces.2009.03.018.
[21] Q. Zhu, M. Heon, Z. Zhao, M. He, Microfluidic engineering of exosomes: editing cellular messages for precision therapeutics, Lab Chip 18 (2018) 1690–1703, https://doi.org/10.1039/C8LC00246K.
[22] M. Wörner, Numerical modeling of multiphase flows in microfluidics and micro process engineering: a review of methods and applications, Microfluid. Nanofluid. 12 (2012) 841–886.
[23] A. Gavriilidis, P. Angeli, E. Cao, K.K. Yeong, Y.S.S. Wan, Technology and applications of microengineered reactors, Chem. Eng. Res. Des. 80 (2002) 3–30, https://doi.org/10.1205/026387602753393196.

[24] M.N. Kashid, A. Renken, L. Kiwi-Minsker, CFD modelling of liquid-liquid multiphase microstructured reactor: slug flow generation, Chem. Eng. Res. Des. 88 (2010) 362–368, https://doi.org/10.1016/j.cherd.2009.11.017.
[25] T. Abadie, C. Xuereb, D. Legendre, J. Aubin, Mixing and recirculation characteristics of gas-liquid Taylor flow in microreactors, Chem. Eng. Res. Des. 91 (2013) 2225–2234, https://doi.org/10.1016/j.cherd.2013.03.003.
[26] R.A. Patil, A. Patnaik, S. Ganguly, A.V. Patwardhan, Effect of structural, thermal and flow parameters on steam reforming of methane in a catalytic microreactor, Chem. Eng. Res. Des. 89 (2011) 2159–2167, https://doi.org/10.1016/j.cherd.2011.01.009.
[27] S. Bettermann, F. Kandelhard, H.U. Moritz, W. Pauer, Digital and lean development method for 3D-printed reactors based on CAD modeling and CFD simulation, Chem. Eng. Res. Des. 152 (2019) 71–84, https://doi.org/10.1016/j.cherd.2019.09.024.
[28] M. Mbodji, J.M. Commenge, L. Falk, Preliminary design and simulation of a microstructured reactor for production of synthesis gas by steam methane reforming, Chem. Eng. Res. Des. 92 (2014) 1728–1739, https://doi.org/10.1016/j.cherd.2013.11.022.
[29] I.L. Chaves, L.C. Duarte, W.K.T. Coltro, D.A. Santos, Droplet length and generation rate investigation inside microfluidic devices by means of CFD simulations and experiments, Chem. Eng. Res. Des. 161 (2020) 260–270.
[30] E. Cimetta, E. Figallo, C. Cannizzaro, N. Elvassore, G. Vunjak-Novakovic, Micro-bioreactor arrays for controlling cellular environments: design principles for human embryonic stem cell applications, Methods 47 (2009) 81–89, https://doi.org/10.1016/j.ymeth.2008.10.015.
[31] O.C. Zienkiewicz, The finite element method: its basis and fundamentals, in: The Finite Element Method: Its Basis and Fundamentals, 2013, iii. https://doi.org/10.1016/b978-1-85617-633-0.00020-4.
[32] P. Mocellin, G. Maschio, Numerical modeling of experimental trials involving pressurized release of gaseous CO_2, Chem. Eng. Trans. 53 (2016) 349–354, https://doi.org/10.3303/CET1653059.
[33] N.-T. Nguyen, S. Wereley, No Title, Artech, 2006. https://ieeexplore.ieee.org/document/9101124.
[34] N. Tandon, D. Marolt, E. Cimetta, G. Vunjak-Novakovic, Bioreactor engineering of stem cell environments, Biotechnol. Adv. 31 (2013) 1020–1031, https://doi.org/10.1016/j.biotechadv.2013.03.007.
[35] J.W. and S.R.B. Bird, W.E. Stewart, E.N. Lightfoot, Transport phenomena, AIChE J. 7 (1961) ^{5}J–^{6}J, New York, 1960, p. 780 pages. https://doi.org/10.1002/aic.690070245.
[36] N.L. Jeon, S.K.W. Dertinger, D.T. Chiu, I.S. Choi, A.D. Stroock, G.M. Whitesides, Generation of solution and surface gradients using microfluidic systems, Langmuir 16 (2000) 8311–8316, https://doi.org/10.1021/la000600b.
[37] S.K.W. Dertinger, D.T. Chiu, N.L. Jeon, G.M. Whitesides, Generation of gradients having complex shapes using microfluidic networks, Anal. Chem. 73 (2001) 1240–1246, https://doi.org/10.1021/ac001132d.
[38] C. Vianello, P. Mocellin, G. Maschio, Study of formation, sublimation and deposition of dry ice from carbon capture and storage pipelines, Chem. Eng. Trans. 36 (2014) 613–618, https://doi.org/10.3303/CET1436103.
[39] D.J. Beebe, G.A. Mensing, G.M. Walker, Physics and applications of microfluidics in biology, Annu. Rev. Biomed. Eng. 4 (2002) 261–286, https://doi.org/10.1146/annurev.bioeng.4.112601.125916.
[40] P.-Y. Gires, Poiseuille et l ' écoulement des liquides dans les capillaires, Bibnum, Sci. l'ingénieur. (2017) 0–11. http://journals.openedition.org/bibnum/1091.
[41] R.K. Shah, A.L. London, Chapter VII - Rectangular ducts, in: R.K. Shah, A.L.B.T.-L.F. F.C. in D. London (Eds.), Academic Press, 1978, pp. 196–222. https://doi.org/https://doi.org/10.1016/B978-0-12-020051-1.50012-7.
[42] B. Atkinson, M.P. Brocklebank, C.C.H. Card, J.M. Smith, Low Reynolds number developing flows, AIChE J. 15 (1969) 548–553, https://doi.org/10.1002/aic.690150414.
[43] E. ~M. Sparrow, C. ~E. Anderson, Effect of upstream flow processes on hydrodynamic development in a duct, ASME J. Fluids Eng. 99 (1977) 556–560.
[44] M. Lake, M. Lake, C. Narciso, K. Cowdrick, T. Storey, S. Zhang, J. Zartman, D. Hoelzle, Microfluidic device design, fabrication, and testing protocols, Protoc. Exch. (2015) 1–26, https://doi.org/10.1038/protex.2015.069.